Journal of Computational and Applied Mathematics 363 (2020) 124–144

Contents lists available at ScienceDirect

Journal of Computational and Applied Mathematics

journal homepage: www.elsevier.com/locate/cam

Remote sensing images destriping using unidirectional hybrid total variation and nonconvex low-rank regularization

Jing-Hua Yang [a], Xi-Le Zhao [a,*], Tian-Hui Ma [b], Yong Chen [a], Ting-Zhu Huang [a], Meng Ding [a]

[a] School of Mathematical Sciences, University of Electronic Science and Technology of China, Chengdu, Sichuan, 611731, PR China
[b] School of Mathematics and Statistics, Xi'an Jiaotong University, Xi'an, Shaanxi 710049, PR China

ARTICLE INFO

Article history:
Received 27 January 2018
Received in revised form 4 September 2018

Keywords:
Destriping
Unidirectional total variation
Unidirectional high-order total variation
Schatten 1/2-norm
Alternating direction method of multipliers

ABSTRACT

In this paper, we propose a novel model for remote sensing images destriping, which includes the Schatten 1/2-norm and the unidirectional first-order and high-order total variation regularization. The main idea is that the stripe layer is low-rank, and the desired image possesses smoothness across stripes. Therefore, we use the Schatten 1/2-norm regularization to depict the low-rankness of stripes, and use the unidirectional total variation and the unidirectional high-order total variation to guarantee the smoothness of the underlying image. We develop the alternating direction method of multipliers algorithm to solve the proposed model. Extensive experiments on synthetic and real data are reported to show the superiority of the proposed method over state-of-the-art methods in terms of both quantitative and qualitative assessments.

1. Introduction

Moderate resolution imaging spectroradiometer (MODIS) images and hyperspectral images are frequently affected by stripe noise, which is a common phenomenon in a large number of spaceborne and airborne multidetector spectrometer imageries [1,2]. Stripe noise has often resulted from the relative error of the calibration of each detector, and the relative gain and offset variations of all detectors. Besides, stripe noise is usually mixed with random Gaussian noise. These undesirable interferences limit applications of the underlying image, such as classification [3], object segmentation [4,5], target detection [6], and scene analysis [7]. Therefore, destriping is indeed considerable and essential preprocessing for remote sensing images. We show in Fig. 1 a destriping example of wide stripe noise, where the local results and the residual error (the difference with the original image and the recovered image) suggest that the proposed method performs well in terms of noise suppression and visual quality.

Traditional destriping methods include filtering-based methods and statistics-based methods. Filtering-based methods perform destriping by a transform-domain filtering, such as Fourier transform [8] and wavelet decomposition [9,10]. These approaches heavily rely on the selection of the transform domain, and may remove the coefficients related to important image details. Statistics-based methods mainly focus on analyzing the distribution of stripes, such as histogram matching [11,12] and moment matching [13]. These methods are time-saving and easy to implement, but they often require that the statistical properties of the digital number for each sensor are the same. Thus, statistics-based methods cannot effectively remove the frequency pulse caused by stripes.

* Corresponding author.
E-mail addresses: 201621100120@std.uestc.edu.cn (J.-H. Yang), xlzhao122003@163.com (X.-L. Zhao), nkmth0307@126.com (T.-H. Ma), chenyong1872008@163.com (Y. Chen), tingzhuhuang@126.com (T.-Z. Huang), dingmeng56@163.com (M. Ding).

https://doi.org/10.1016/j.cam.2019.06.004
0377-0427/

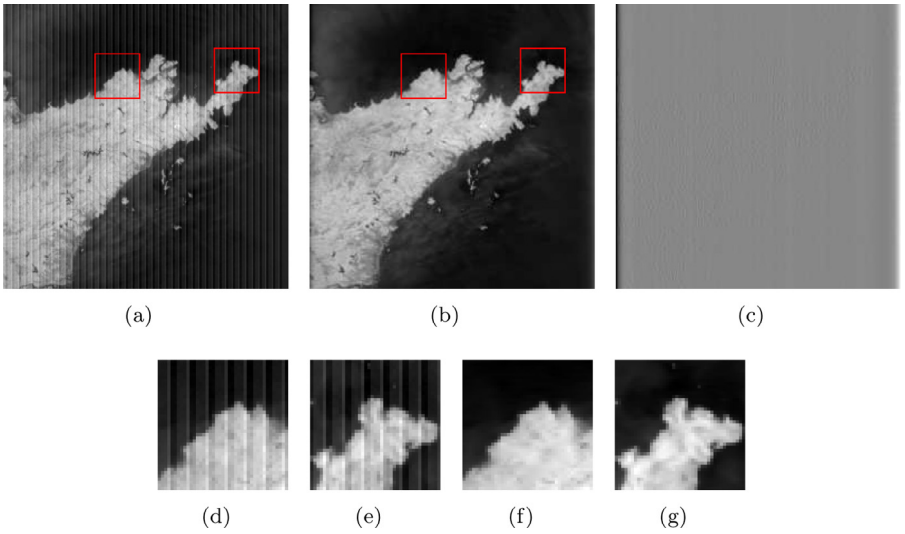

Fig. 1. An example of removing wide stripe noise (three lines together). Top row from left to right: the degraded image, result by the proposed method, and the residual image. Bottom row: zoomed-in results of (a) and (b).

Destriping is regarded as an inverse problem whose solution is usually ill-posed. Thus, regularization methods have received much attention for stripe noise removal. The main idea is to restrain the solution space according to a prior knowledge [14–19]. Based on an edge-preserving Huber–Markov image prior, Shen and Zhang [20] proposed a maximum a posteriors (MAP)-based method for destriping. By exploiting the direction signature of stripes, Bouali and Ladjal [21] proposed a variational algorithm by introducing a unidirectional total variational model (UTV) for MODIS image destriping. For further improvement, Zhou et al. [22] introduced a robust hybrid UTV model with two combined l_1 data-fidelity to handle stripe noise of MODIS and hyperspectral images. Chang et al. [23] proposed a joint UTV and framelet regularization method to address destriping problems, where they used the total variation (TV) to remove stripe noise effectively and framelet to preserve image details.

Although the aforementioned methods achieve satisfactory performance, they ignore the structure prior to stripe noise. Recently, to conquer this drawback, some works aim at exploiting the structure feature of stripe noise. Liu et al. [24] used the l_0-norm-based regularization to characterize the global sparse distribution of stripes, but the sparsity assumption is not satisfied when stripes are too dense. Chen et al. [25] utilized the $l_{2,1}$-regularization to characterize the group sparsity of stripes, and adopted TV regularization to explore the spatial piecewise smooth structure of images. Chang et al. [26] analyzed the low-rankness of stripes and used the nuclear norm to extract stripe noise. These destriping methods achieve excellent performance on thin and regular stripes, but they cannot effectively remove agminated, banding, and irregular stripes while producing the staircase effect in destriping images. In addition, they do not fully exploit the directional and structural characteristics of stripes, especially when removing wide stripes. In summary, there leaves plenty of room for future investigation on improving the performance and the application range of destriping methods.

In this paper, we propose a novel destriping model based on the Schatten 1/2-norm, UTV, and the unidirectional high-order total variation (UHTV) regularization by exploring the intrinsically directional and structural features of stripes. Our motivation has two folds. First, the image layer is smooth in the vertical direction of stripe noise (see Fig. 2), thus UTV and UHTV are used to restrain the smooth subspace while reducing the staircase effect. Second, the stripe noise is approximately rank-one, as shown the singular value decomposition in Fig. 2, so the Schatten 1/2-norm is used to characterize the low-rankness of stripe noise. To the best of our knowledge, there is no work using UHTV for the destriping problem. An efficient alternating direction method of multipliers (ADMM)-based algorithm is designed to solve the proposed model. The main contributions of the proposed method are summarized below.

1. We use UTV and UHTV to alleviate staircase effects of the estimated image. Moreover, they also help to exclude the stripes along the vertical direction in the estimated image.

2. We use the Schatten 1/2-norm to characterize the low-rankness of stripes; meanwhile, it also has a simple closed-form solution [27].

The remainder of this paper is organized as follows. In Section 2, we present the proposed model and some prior knowledge by fully considering the structure and the direction of stripes. In Section 3, the ADMM-based optimization algorithm is formulated. In Section 4, we show extensive experimental results on simulated and real data to confirm the effectiveness and robustness of the proposed method. In Section 5, we discuss the effects of regularization terms and regularization parameters to restored results, and numerically demonstrate the convergence of the proposed algorithm. In Section 6, we conclude this paper.

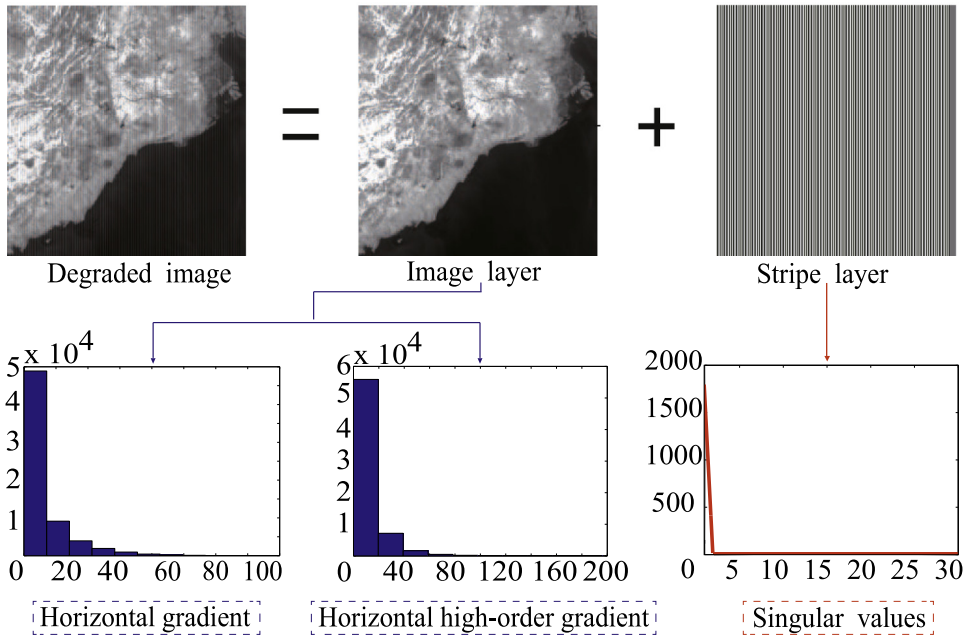

Fig. 2. Framework of the proposed method. The degraded image is decomposed into the image layer and the stripe layer (top row). After analyzing the first-order and high-order gradients of the image layer and singular values of the stripe layer, they have different distinct properties or characteristics (bottom row). Thus, the image layer and the stripe layer are projected to smooth subspace and low-rank subspace, respectively.

2. The proposed model

In this Section, we propose a new destriping model based on the low-rank prior, UTV, and UHTV. The stripes effect is considered as additive noise in remote sensing images [21], so the degradation model can be written as

$$Y = U + S + N, \tag{1}$$

where Y, U, S, and $N \in R^{m\times n}$ denote the observed image, the desired data, the additive stripe component, and the Gaussian white noise with rows and columns as $m \times n$, respectively.

We use UTV and UHTV to restrain the smooth subspace and use the Schatten 1/2-norm to characterize the low-rankness of stripe noise, so our model is formulated by

$$\arg\min_{U,S} \frac{1}{2}\|U + S - Y\|_F^2 + \lambda_1\|S\|_{s_{1/2}}^{1/2} + \lambda_2\|D_x U\|_1 + \lambda_3\|D_{xx}^2 U\|_1, \tag{2}$$

where $\|U + S - Y\|_F^2$ is the data-fidelity term, the last three terms are the regularization terms, $\|S\|_{s_{1/2}}^{1/2} = \sum_{i=1}^{r}\sigma_i^{1/2}$ (Schatten 1/2-norm) represents the $L_{1/2}$ quasi-norm of all the singular values $\{\sigma_i\}_{i=1}^r$ of the matrix S, D_x and D_{xx}^2 denote the first-order gradient operator and the high-order gradient operator across stripes direction, respectively, $\|\cdot\|_1$ represents the sum of absolute value of all elements, λ_1, λ_2, and λ_3 are the regularization parameters. In the following sections, we give the motivation for each regularization term.

2.1. UTV and UHTV

The TV-based regularization has been widely used in various applications, owing to its desirable edge-preserving property [28–32]. Fig. 3 presents the directional gradients for the degraded image and the original image (e.g., MODIS). It is worth noting that the gradients along stripes are not affected by stripe lines, but the horizontal gradients are absolutely different. Furthermore, compared with the intensities of a random row in Fig. 3(f) and (i), we find that stripes mainly damage the sparseness of the horizontal gradient of the original image, which implies the smoothness along the horizontal direction in the estimated image. Therefore, we use UTV to preserve the sharp edges and the piece-wise smoothness of the original image.

TV-based recovery methods usually have the staircase effect [33–36]. For wide stripes, high-order TV (HTV) can maintain the smoothness of the image better than TV, while reducing the staircase effect. Taking vertical stripes as an example, we show the high-order gradients of the degraded image and the original image in Fig. 4, respectively. These

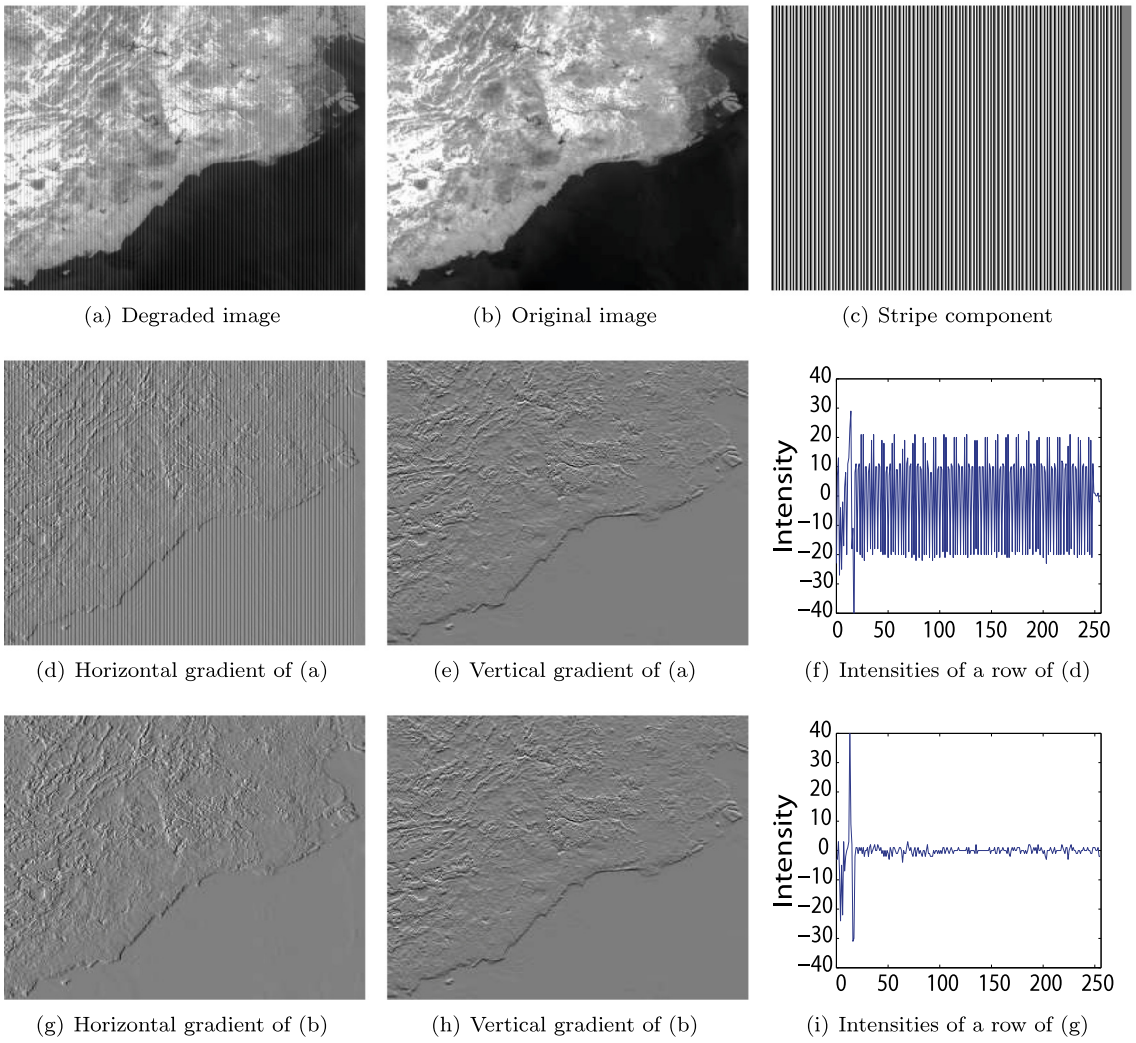

(a) Degraded image (b) Original image (c) Stripe component

(d) Horizontal gradient of (a) (e) Vertical gradient of (a) (f) Intensities of a row of (d)

(g) Horizontal gradient of (b) (h) Vertical gradient of (b) (i) Intensities of a row of (g)

Fig. 3. The directional gradients for the degraded image and the original image. This figure shows that the stripes only affect the horizontal gradient of the desired image.

images suggest that the stripes mainly damage the smoothness of the desired image along the *xx*-direction. Therefore, it is reasonable to use UHTV to keep the high-order smoothness of the image and reduce the staircase effect caused by TV. [High-order Gradients: $D^2U = \begin{pmatrix} D_{xx}U & D_{xy}U \\ D_{yx}U & D_{yy}U \end{pmatrix}$.]

2.2. Schatten 1/2*-norm*

Next, we study the structure property of stripe noise. Fig. 2 shows that stripe noise is approximately rank-one. Since direct rank minimization is NP-hard and is difficult to solve, it is generally relaxed by nuclear norm minimization. However, the nuclear norm is a biased approximation of the rank, which leads to suboptimal solutions [37]. From Fig. 5, it is easy to observe that $L_{1/2}$ quasi-norm approximates the matrix rank better than the nuclear norm. So, we apply the Schatten 1/2-norm to restrain the low-rankness of stripes.

3. The ADMM algorithm

In this Section, we design an effective algorithm to solve the proposed model based on ADMM [38–41], which is an effective strategy for solving large-scale optimization problems. The proposed model (2) forms the following equivalent

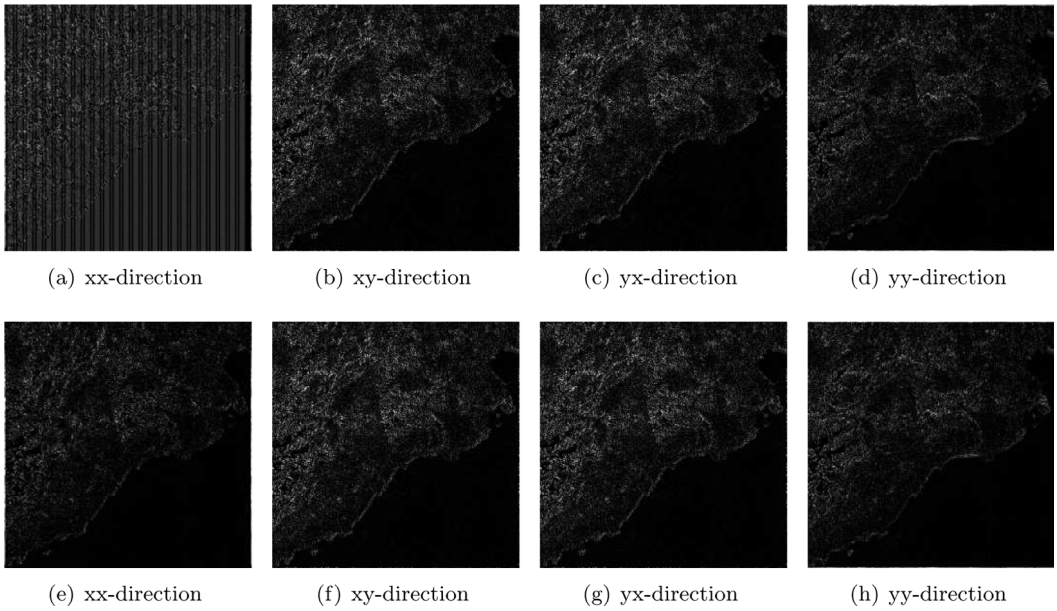

Fig. 4. The high-order directional gradients for the degraded image and the original image (undergo a same linear enhancement for better visualization). This figure shows that the stripes mainly damage the smoothness of the desired image along the xx-direction.

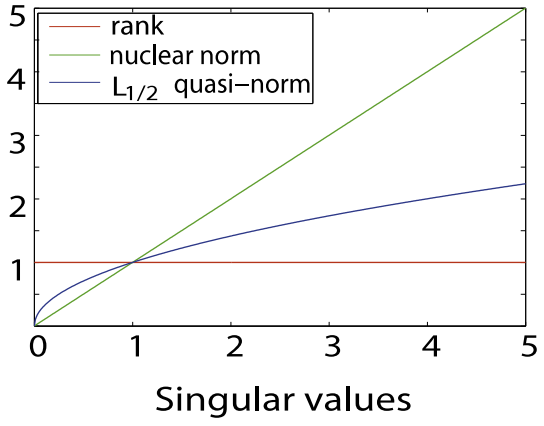

Fig. 5. Approximation of the rank function using different functions.

constrained problem by introducing three auxiliary variables $D_1 = S, D_2 = D_xU, D_3 = D_{xx}^2U$:

$$\begin{aligned} E(U,S) =& \frac{1}{2}\|U+S-Y\|_F^2 + \lambda_1\|D_1\|_{s_{1/2}}^{1/2} + \lambda_2\|D_2\|_1 + \lambda_3\|D_3\|_1, \\ & s.t. \qquad D_1 = S, D_2 = D_xU, D_3 = D_{xx}^2U, \end{aligned} \tag{3}$$

where $\|D_1\|_{s_{1/2}}^{1/2}$ is the Schatten 1/2-norm (see formula 2) of the variable D_1. The augmented Lagrangian function of (3) is given by

$$\begin{aligned} L(U,S,D_1,D_2,D_3,J_1,J_2,J_3,) =& \frac{1}{2}\|U+S-Y\|_F^2 + \lambda_1\|D_1\|_{s_{1/2}}^{1/2} + \lambda_2\|D_2\|_1 + \lambda_3\|D_3\|_1 \\ +& \frac{\delta}{2}\|D_1 - S - \frac{J_1}{\delta}\|_F^2 + \frac{\gamma}{2}\|D_2 - D_xU - \frac{J_2}{\gamma}\|_F^2 + \frac{c}{2}\|D_3 - D_{xx}^2U - \frac{J_3}{c}\|_F^2, \end{aligned} \tag{4}$$

where J_1, J_2, and J_3 are Lagrangian multipliers and δ, γ, and c are penalty parameters. Then ADMM iterates as follows:

$$\begin{cases} (U^{k+1}, S^{k+1}) = \arg\min_{U,S} L(U, S, D_1^k, D_2^k, D_3^k, J_1^k, J_2^k, J_3^k), \\ (D_1^{k+1}, D_2^{k+1}, D_3^{k+1}) = \arg\min_{D_1,D_2,D_3} L(U^{k+1}, S^{k+1}, D_1, D_2, D_3, J_1^k, J_2^k, J_3^k), \\ J_1^{k+1} = J_1^k + \delta(D_1^{k+1} - S^{k+1}), \\ J_2^{k+1} = J_2^k + \gamma(D_2^{k+1} - D_x U^{k+1}), \\ J_3^{k+1} = J_3^k + c(D_3^{k+1} - D_{xx}^2 U^{k+1}), \end{cases} \tag{5}$$

Below we give the details of solving each subproblem.

• (U, S)-**subproblem.** The (U, S)-subproblem is

$$\begin{aligned} (U^{k+1}, S^{k+1}) = \arg\min_{U,S} & \frac{1}{2}\|U + S - Y\|_F^2 + \frac{\delta}{2}\|D_1^k - S - \frac{J_1^k}{\delta}\|_F^2 \\ & + \frac{\gamma}{2}\|D_2^k - D_x U - \frac{J_2^k}{\gamma}\|_F^2 + \frac{c}{2}\|D_3^k - D_{xx}^2 U - \frac{J_3^k}{c}\|_F^2. \end{aligned} \tag{6}$$

The solution satisfies the following normal equation:

$$\begin{bmatrix} P & I \\ I & I + \delta I \end{bmatrix} \begin{bmatrix} U \\ S \end{bmatrix} = \begin{bmatrix} Q \\ Y + \delta I(D_1^k - \frac{J_1^k}{\delta}) \end{bmatrix}, \tag{7}$$

where $P = I + \gamma D_x^T D_x + c(D_{xx}^2)^T D_{xx}^2$ and $Q = Y + \gamma D_x^T(D_2^k - \frac{J_2^k}{\gamma}) + c(D_{xx}^2)^T(D_3^k - \frac{J_3^k}{c})$. It can be solved efficiently in the Fourier domain as in [28].

• (D_1, D_2, D_3)-**subproblem.** Since D_1, D_2, and D_3 are decoupled with each other, they can be solved separately.

(1) D_1-subproblem

$$D_1^{k+1} = \arg\min_{D_1} \lambda_1 \|D_1\|_{s_{1/2}}^{1/2} + \frac{\delta}{2}\|D_1 - S^{k+1} - \frac{J_1^k}{\delta}\|_F^2 \tag{8}$$

has the following closed-form solution by Half threshold operator [42,43]:

$$D_1^{k+1} = U H_\lambda(\Sigma) V^T, \tag{9}$$

where $S^{k+1} + \frac{J_1^k}{\delta} = U\Sigma V^T$ is the singular value decomposition of $S^{k+1} + \frac{J_1^k}{\delta}$, $\Sigma = \mathrm{diag}(\sigma_1, \sigma_2, \ldots, \sigma_r)$, U and V are $m \times r$ and $n \times r$ matrices with orthonormal columns, respectively, $\lambda = \frac{2\lambda_1}{\delta}$, and

$$H_\lambda(x) = \begin{cases} \frac{2}{3}x(1 + \cos(\frac{2\Pi}{3} - \frac{2\varphi(x)}{3})), & |x| > \frac{\sqrt[3]{54}}{4}\lambda^{\frac{2}{3}}, \\ 0, & \text{others}, \end{cases}$$

($\varphi(x) = \arccos(\frac{\lambda}{8}(\frac{|x|}{3})^{-\frac{3}{2}})$).

(2) D_2-subproblem

$$D_2^{k+1} = \arg\min_{D_2} \lambda_2 \|D_2\|_1 + \frac{\gamma}{2}\|D_2 - D_x U^{k+1} - \frac{J_2^k}{\gamma}\|_F^2 \tag{10}$$

has the following closed-form solution by the soft shrinkage operator [44,45]:

$$D_2^{k+1} = \max(|D_x U^{k+1} + \frac{J_2^k}{\gamma}| - \frac{\lambda_2}{\gamma}, 0) \circ \frac{D_x U^{k+1} + \frac{J_2^k}{\gamma}}{|D_x U^{k+1} + \frac{J_2^k}{\gamma}|}, \tag{11}$$

where $\circ$ denotes component-wise multiplication and the division is also performed component-wise. The convention $0 \circ \frac{0}{0} = 0$ is assumed.

(3) D_3-subproblem

$$D_3^{k+1} = \arg\min_{D_3} \lambda_3 \|D_3\|_1 + \frac{c}{2}\|D_3 - D_{xx}^2 U^{k+1} - \frac{J_3^k}{c}\|_F^2 \tag{12}$$

can be similarly solved by

$$D_3^{k+1} = \max(|D_{xx}^2 U^{k+1} + \frac{J_3^k}{c}| - \frac{\lambda_3}{c}, 0) \circ \frac{D_{xx}^2 U^{k+1} + \frac{J_3^k}{c}}{|D_{xx}^2 U^{k+1} + \frac{J_3^k}{c}|}. \tag{13}$$

Therefore, the ADMM algorithm for solving the proposed model is summarized as follows:

Algorithm 1 : **The alternating direction method with multipliers for solving** (2).

Input: data Y, parameters λ_1, λ_2, λ_3.
Initialize: $U = Y$, $S = 0$, D_1, D_2, D_3, J_1, J_2, J_3, $\epsilon = 1e-5$, $maxiter = 300$.
1: **While** ($\|U^{k+1} - U^k\|_F / \|U^k\|_F > \epsilon$ and $k \leq maxiter$) **Do**
2: Update (U^{k+1}, S^{k+1}) by (7).
3: Update D_1^{k+1} by (9).
4: Update D_2^{k+1} and D_3^{k+1} by (11) and (13), respectively.
5: Update J_1^{k+1}, J_2^{k+1}, and J_3^{k+1} by (5), respectively.
6: **End Do**
Output: Restored image U^{k+1} and stripe noise S^{k+1}.

4. Experiments

Section 4.1 gives experimental settings. Sections 4.2 and 4.3 present destriping experiments using simulated data and real data, respectively.

4.1. Experimental setting

We compare our method with the unidirectional total variational model [21] (denoted as UTV) and the low-rank-based single-image decomposition model [26] (denoted as LRSID). We choose these competing methods because they consider both direction property and structure property of stripe noise, which makes the comparison persuasive and comprehensive.

Stripe generation. For simulated data, we generate the degraded images by the following steps. First, the original images are coded to an 8-bit scale. Second, stripes with intensity [0, 255] and tiny (0.01) Gaussian white noise are added to the original images. Third, the striped images are normalized to [0, 1]. For simplicity, different stripes added to remote sensing images will be denoted as a vector with three elements, e.g., (Per/Non-Per, intensity, r), where 'Per/Non-Per' denotes periodical stripes or nonperiodical stripes, 'intensity' denotes the absolution value of the added stripes, and 'r' represents the stripe ratio within the image.

Qualitative and quantitative indices. For simulated data, we use the visual impact and the mean cross-track profile (x-axis stands for the column number of the image, and the y-axis represents the mean value of each column) as qualitative indices of the restored image. Since the ground-truth image is available, we use quantitative indices including the peak signal-to-noise ratio (PSNR) [46] and the structural similarity index (SSIM) [47] to evaluate the quality of the restored image, which are defined as follows:

$$\text{PSNR} = 10\log_{10}\frac{mn(\max_U)^2}{\|U - U^*\|_F^2},$$
$$\text{SSIM} = \frac{(2\mu_U\mu_{U^*})(2\sigma_{UU^*} + c_2)}{(\mu_U^2 + \mu_{U^*}^2 + c_1)(\sigma_U^2 + \sigma_{U^*}^2 + c_2)},$$

where U^* is the true image, U is the recovered image, $\max_U$ is the maximum pixel of the image, μ_U and μ_{U^*} are the mean values of images U and U^*, σ_U and σ_{U^*} are the standard variances of U and U_*, respectively, σ_{UU^*} is the covariance of U and U^*, and $c_1, c_2 > 0$ are constants. Higher PSNR and SSIM values imply better image quality.

For real data, since the ground-truth is unknown, we choose no-reference evaluation indices including noise reduction (NR) [1,20], mean relative deviation (MRD) [1,20], and the inverse coefficient of variation (ICV) [20]. NR measures the effectiveness of stripe removal, ICV evaluates the level of removing stripe noise, and MRD measures the distortion of the original image caused by the adopted destriping method. Higher values of NR and ICV mean a better destriping performance, and lower values of MRD mean better image detail preservation. In addition, the qualitative assessments include the mean cross-track profile and power spectrum (x-axis is the normalized frequencies of the image, and the y-axis denotes the mean power spectrum of all rows in the image with a logarithmic scale).

Parameter setting. Regularization parameters λ_1, λ_2, and λ_3 in (2) balance the data fidelity and the regularization terms. The hand-tuned strategy is used for these parameters. We empirically set their ranges as $\lambda_1 \in [0, 1]$, $\lambda_2 \in [0.0001, 0.01]$, $\lambda_3 \in [0.0001, 0.01]$, and penalty parameters (δ, γ, and c) in the range of [0.00001, 0.01] and optimize them to attain the highest PSNR value in the simulated experiments or the best visual performance in the real experiments. For the compared methods, the parameters are set as the suggested values in the references.

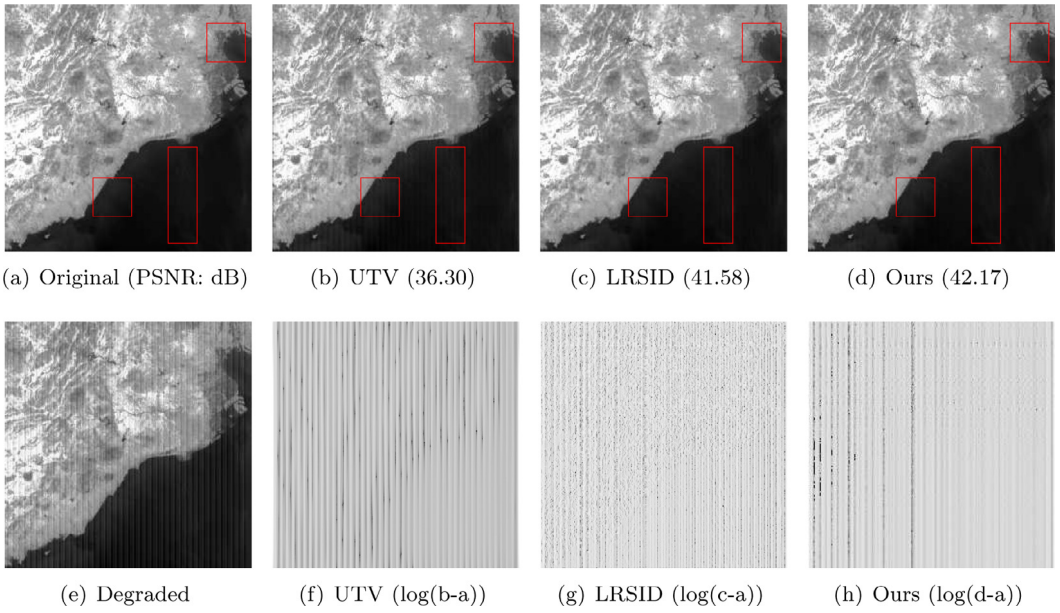

(a) Original (PSNR: dB) (b) UTV (36.30) (c) LRSID (41.58) (d) Ours (42.17)

(e) Degraded (f) UTV (log(b-a)) (g) LRSID (log(c-a)) (h) Ours (log(d-a))

Fig. 6. Destriping results for the three lines together case (intensity = 10) (each value in parentheses represents the corresponding PSNR value of the restored image). Top row: the original image and recovered images. Bottom row: the degraded image and residual error images.

4.2. Simulated data

In our simulated experiments, we test the proposed method on two kinds of stripe cases: periodical stripes and nonperiodical stripes. The hyperspectral image of Washington DC Mall[1] and MODIS image[2] band 32 are used to assess the performance of the proposed method.

(1) **Periodical stripes**. We simulate periodic stripes that every three and two lines are grouped and the absolute value of the stripe line pixels is the same. Fig. 6 shows the destriping results of three lines together. It can be observed clearly that UTV has relatively poor performance with obvious residual stripes, see Fig. 6(b). At the same time, some boundaries are blurred after destriping by LRSID, and there still exists residual stripes in the restored result, see Fig. 6(c). In contrast, the proposed method shows better visual performance. For a more objective assessment, residual error images (the logarithm operation of the difference with the original image and recovered image) are presented. The residual error of the proposed method has fewer stripes information and details information. Besides, in Fig. 7, we plot the intensities of a random row of Fig. 6. In comparison, the curve produced by the proposed method holds almost the same curve as the original one. It demonstrates that the proposed method can reduce staircase artifacts.

Figs. 8 and 9 show the destriping images and the estimated stripes of different methods for thin stripes (Per, 50, 0.2) and wide stripes (Per, 10, 0.8) removal. We can view that the competing methods exhibit residual stripes and blur effects. The proposed method precisely extracts the stripe component, without losing image structures or bringing blur effects. From the mean comparison of Fig. 8(j), the estimated stripe component obtained by the proposed method is the closest to the original one, especially in the stripe-free regions.

Fig. 10 shows the column mean cross-track profiles of Figs. 6 and 9 as examples. There are many residual stripes existing in the image by UTV, so column mean cross-track profile curve has a large rise and fall (see Fig. 10(b)). Meanwhile, compared with the original mean cross-track profile, LRSID has too many spines. The column mean cross-track profile of the proposed method has almost the same curve as the original one, which is consistent with the visual analysis. The above observations also hold for other periodical stripes experiments.

(2) **Nonperiodical stripes**. Figs. 11 and 12 present the destriping results for nonperiodic thin stripes (Non-Per, 10, 0.2) and wide stripes (Non-Per, 10, 0.8), respectively. The proposed method can resolve the residual stripes issue without introducing blurring. On the contrary, for wide stripes, LRSID method overlooks much texture information by blurring images, see Fig. 12(d). Meanwhile, from the stripe components in Figs. 11 and 12, our method precisely estimates and separates the true stripe components.

(3) **Quantitative assessment**. Tables 1–3 show the PSNR (dB) and SSIM values of the simulated experiments. The results suggest that our method achieves the highest PSNR and SSIM values in most cases. The results of Tables 1–3 are consistent with the visual comparison.

1 https://engineering.purdue.edu/biehl/MultiSpec/hyperspectral.html.

2 https://ladsweb.nascom.nasa.gov/.

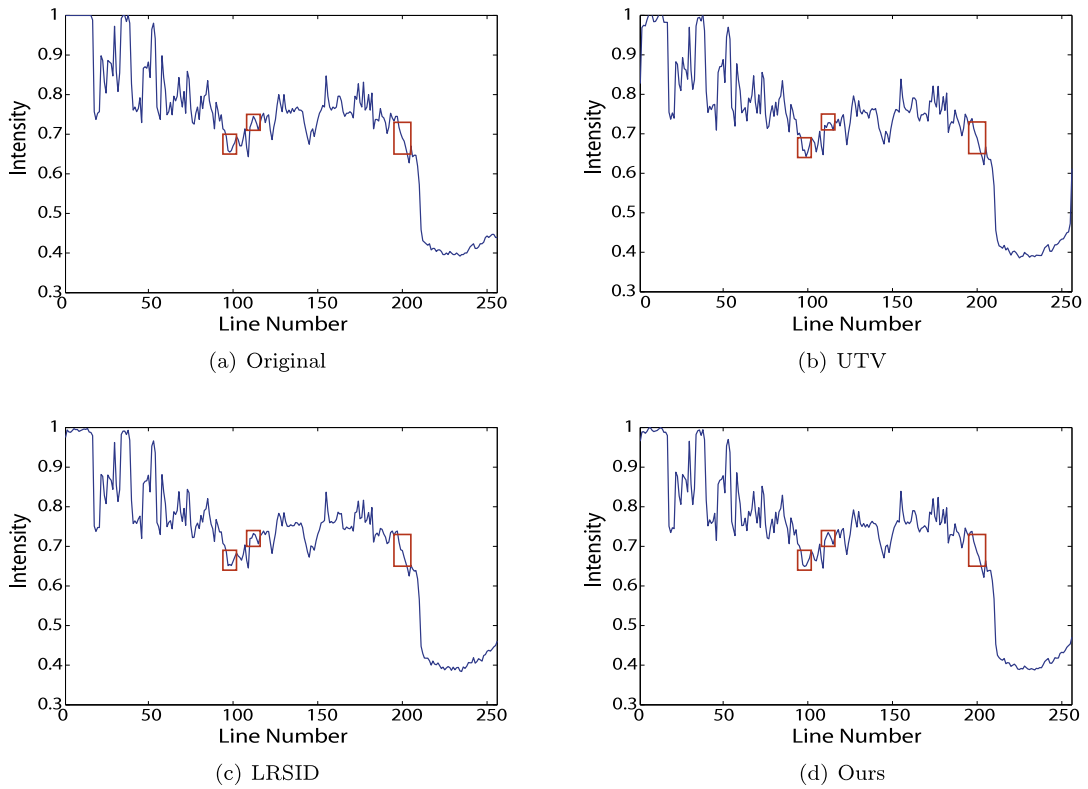

Fig. 7. An example of reducing staircase effects.

Table 1
PSNR (dB) and SSIM results of the test methods for stripe noise of two lines and three lines together.

Stripe noise	Image	Method	Intensity = 10		Intensity = 50		Intensity = 0–50		Intensity = 100	
			PSNR	SSIM	PSNR	SSIM	PSNR	SSIM	PSNR	SSIM
Two lines together	Hyperspectral Periodical Image	Degraded	32.97	0.939	19.00	0.502	24.06	0.743	12.97	0.244
		UTV	43.43	0.998	39.15	0.994	**37.88**	0.994	36.91	0.990
		LRSID	42.24	0.994	38.31	0.989	36.91	0.991	37.76	0.990
		Proposed	**45.89**	**0.998**	**40.55**	**0.994**	37.76	**0.994**	**39.31**	**0.994**
	MODIS Periodical Image	Degraded	32.97	0.815	18.91	0.234	24.06	0.501	12.97	0.083
		UTV	37.76	0.994	35.98	0.985	34.56	**0.992**	34.81	0.976
		LRSID	44.30	0.993	41.41	0.985	37.29	0.984	41.06	0.986
		Proposed	**46.35**	**0.995**	**43.92**	**0.993**	**38.52**	0.991	**42.38**	**0.994**
Three lines together	Hyperspectral Periodical Image	Degraded	31.21	0.918	17.23	0.417	22.33	0.689	11.21	0.170
		UTV	38.63	0.994	28.67	0.974	32.03	0.983	23.27	0.935
		LRSID	39.03	0.991	29.18	0.981	32.44	0.984	23.47	0.937
		Proposed	**40.40**	**0.996**	**29.23**	**0.985**	**33.24**	**0.991**	**23.60**	**0.954**
	MODIS Periodical Image	Degraded	31.21	0.765	17.23	0.178	22.33	0.437	11.21	0.057
		UTV	36.30	0.987	28.67	0.982	29.31	0.878	23.35	0.959
		LRSID	41.58	0.991	29.50	0.982	**32.46**	0.974	**23.63**	0.952
		Proposed	**42.17**	**0.998**	**29.51**	**0.991**	32.18	**0.990**	23.58	**0.985**

In summary, the proposed method provides better qualitative and quantitative results.

4.3. Real data

The proposed method is tested on three real MODIS data sets[3] for destriping, see Fig. 13. For horizontal stripe noise, we transpose them into vertical stripes for processing.

[3] https://compression.jpl.nasa.gov/hyperspectral/imagedata/.

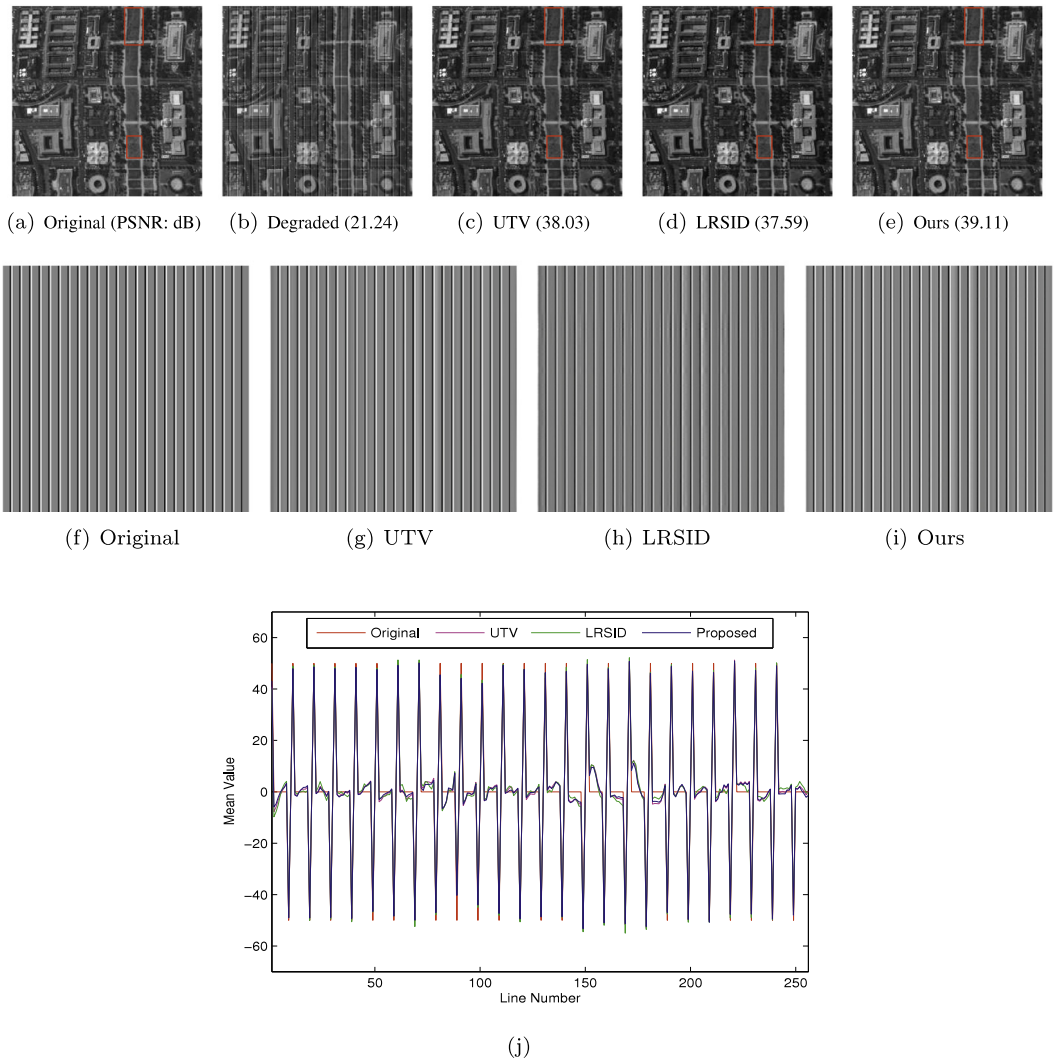

Fig. 8. Destriping results for the simulated periodic thin stripes case (Per, 50, 0.2) (each value in parentheses represents the corresponding PSNR value of the restored image). Top row: the original image and recovered images. Middle row: stripe components. Bottom row: mean comparison (j) between the stripes estimated by the original added, UTV, LRSID, and the proposed method.

(1) **Periodical stripes**. Fig. 14 shows the destriping results of band 30 and band 27 of the Terra MODIS data as examples of periodic stripes. In comparison, the proposed method can achieve a better destriping performance. Clearly, UTV and LRSID both bring varying degrees of blur to useful information in the destriping process.

Fig. 15 presents the stripe components. It is clear that UTV extracts additional background information on the stripe component. Due to the emergence of the blur, the stripe component of LRSID damages the partial structures. A visual assessment clearly shows that the proposed approach can separate the complete stripe component.

Fig. 16 shows the mean cross-track profiles before and after destriping. The mean cross-track profile of UTV method is over-smoothing, indicating some fine details are simultaneously smoothed. On the contrary, the LRSID method provides a barbed curve. By comparison, the proposed method is neither over smooth nor loss of details information.

Fig. 17 shows the power spectrum results. For the proposed method, which not only can remove all stripes, but also preserve the essential details. In fact, UTV provides a good smoothing of the power spectrum curve but at the cost of a blur of details from the original images.

(2) **Nonperiodical stripes**. Fig. 18 shows the experiment results of the nonperiodical stripes image. In this case, LRSID shows a better performance. However, it pays the price of losing the details of the image, as shown the estimated stripes in Fig. 18(n). In addition, the column mean cross-track profiles and the power spectrum curves of UTV are over smoothed, while LRSID has many small spines. This demonstrates that UTV and LRSID damage useful information in the destriping process, whereas the proposed method removes the noise component much more accurately and preserves useful information completely.

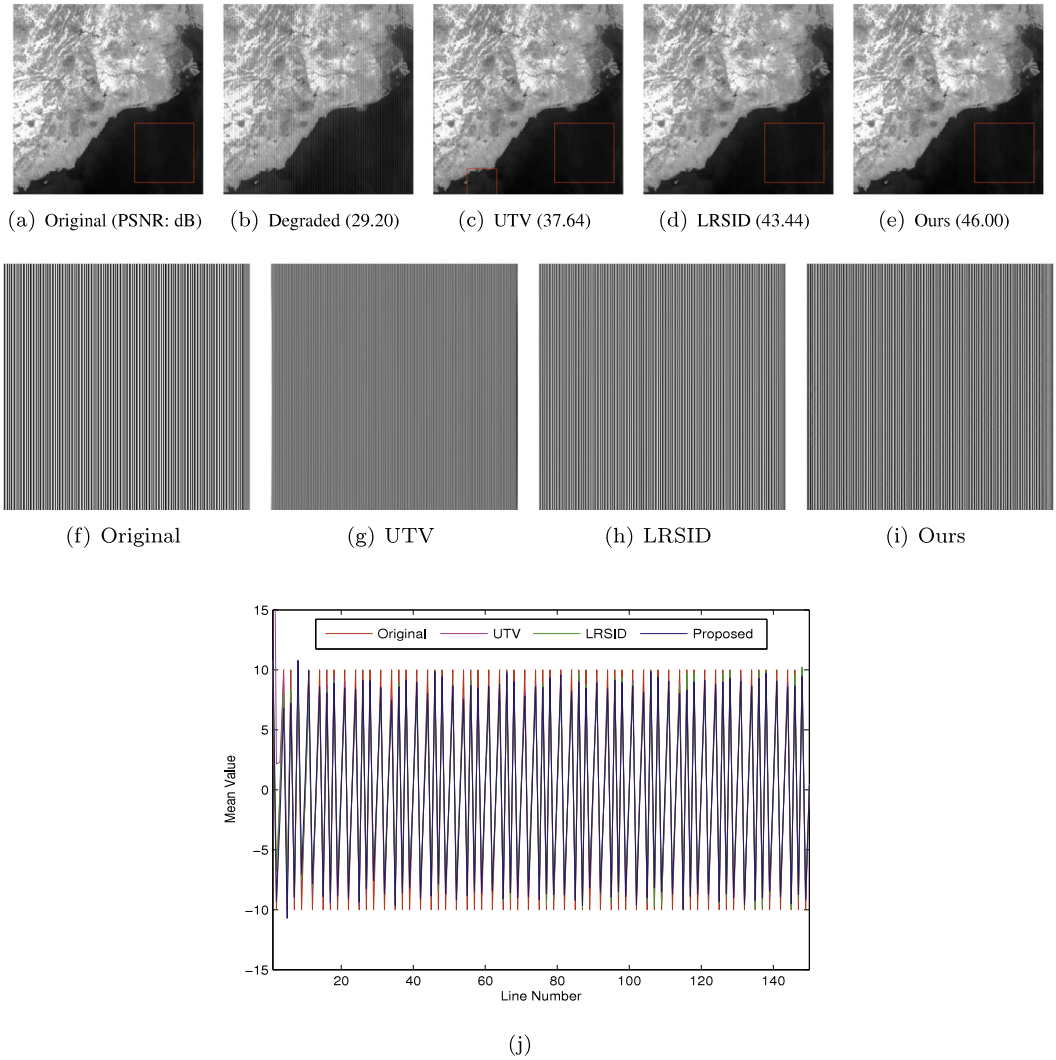

Fig. 9. Destriping results for the simulated periodic wide stripes case (Per, 10, 0.8) (each value in parentheses represents the corresponding PSNR value of the restored image). Top row: the original image and recovered images. Middle row: stripe components. Bottom row: mean comparison (j) between the stripes estimated by the original added, UTV, LRSID, and the proposed method.

(3) **Quantitative assessment**. Table 4 presents the MRD, NR, and ICV evaluation results of different methods. Although UTV achieves the highest NR and ICV values from the Terra MODIS band 30, it pays the price of removing much important texture information in the resulting images. In comparison, the proposed method can simultaneously obtain competitive values and provide high-quality destriped images. Although our method is slightly slower than compared methods, our method achieves the better result in terms of both quantitative and qualitative assessments.

5. Discussions

In this Section, we will discuss the effects of the regularization terms and the regularization parameters in our model.

5.1. Regularization terms

In our method, the low-rankness of stripe component, the along-stripe smoothness, and the across-stripe discontinuity as constraint terms simultaneously estimate the stripe layer and the image layer. To study the role of each regularization term, we show different settings of regularization terms in Fig. 19. Compared the residual errors (the difference with the original image and the recovered image) with Fig. 19(f) and (h), there are many obvious residual stripes in Fig. 19(f). It demonstrates that UHTV is necessary to keep the smoothness of the image and exclude the wide stripe noise. While

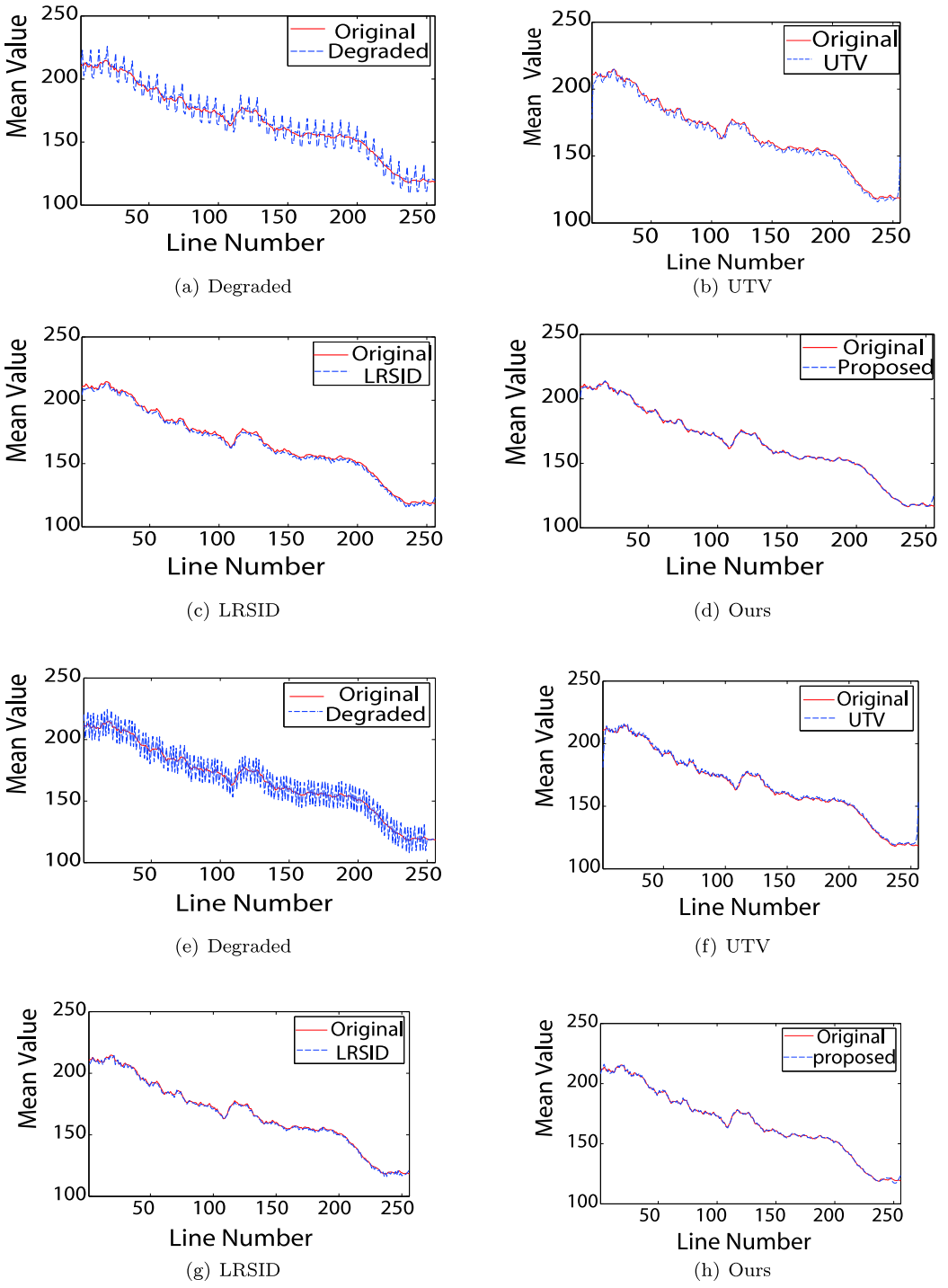

Fig. 10. The first two rows: column mean cross-track profiles of Fig. 6. The last two rows: column mean cross-track profiles of Fig. 9.

compared with Fig. 19(g) and (h), Fig. 19(g) contains a lot of details, which proves that the Schatten 1/2-norm is more precise for depicting the low-rankness compared with the nuclear norm. Therefore, by combining UTV, UHTV, and the Schatten 1/2-norm constraints into the optimization problem, our method can recover clear images almost without residual stripes. In summary, we demonstrate that UHTV is effective to alleviate the staircase effect so as to keep the smoothness of the image, and the Schatten 1/2-norm can accurately describe the structure property of stripe noise.

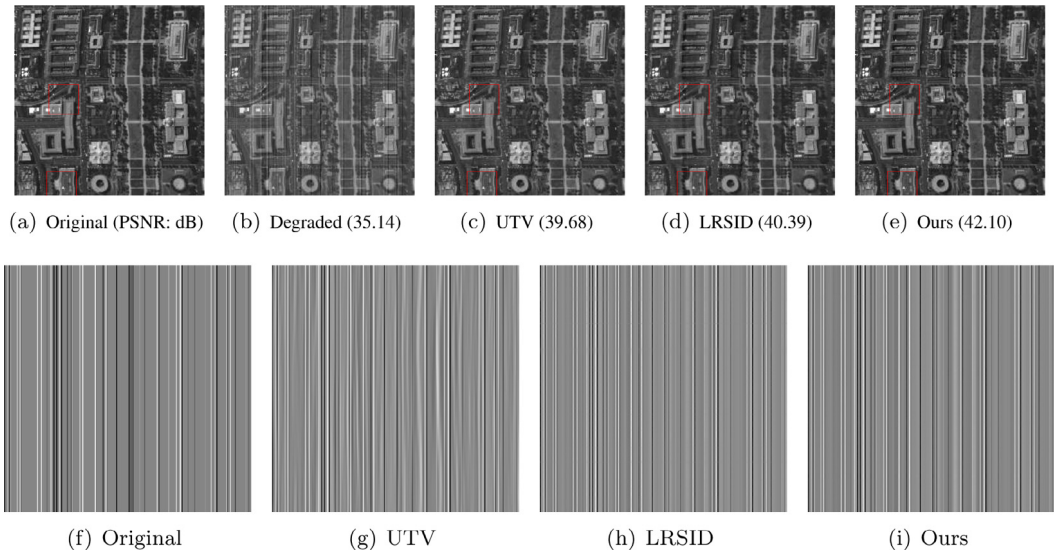

Fig. 11. Destriping results for the simulated nonperiodic thin stripes case (Non-Per, 10, 0.2) (each value in parentheses represents the corresponding PSNR value of the restored image). Top row: the original image and recovered images. Bottom row: stripe components.

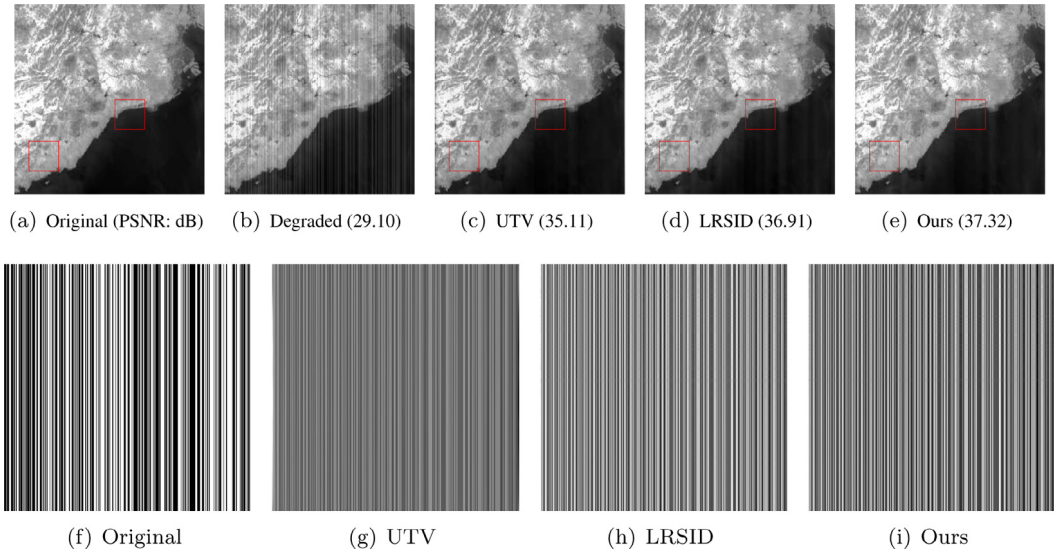

Fig. 12. Destriping results for the simulated nonperiodic wide stripes case (Non-Per, 10, 0.8) (each value in parentheses represents the corresponding PSNR value of the restored image). Top row: the original image and recovered images. Bottom row: stripe components.

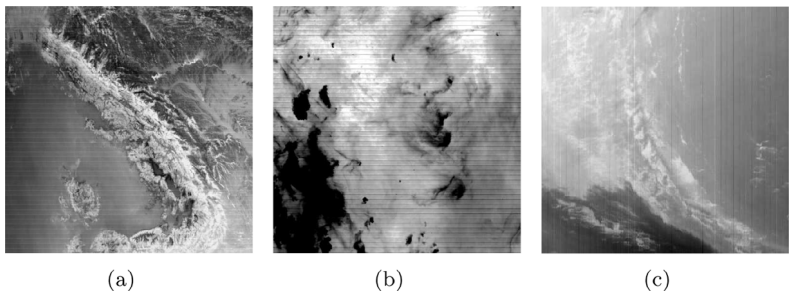

Fig. 13. The real data: (a) Terra MODIS band 30 (periodic); (b) Terra MODIS band 27 (periodic); (b) Terra MODIS band 33 (nonperiodic).

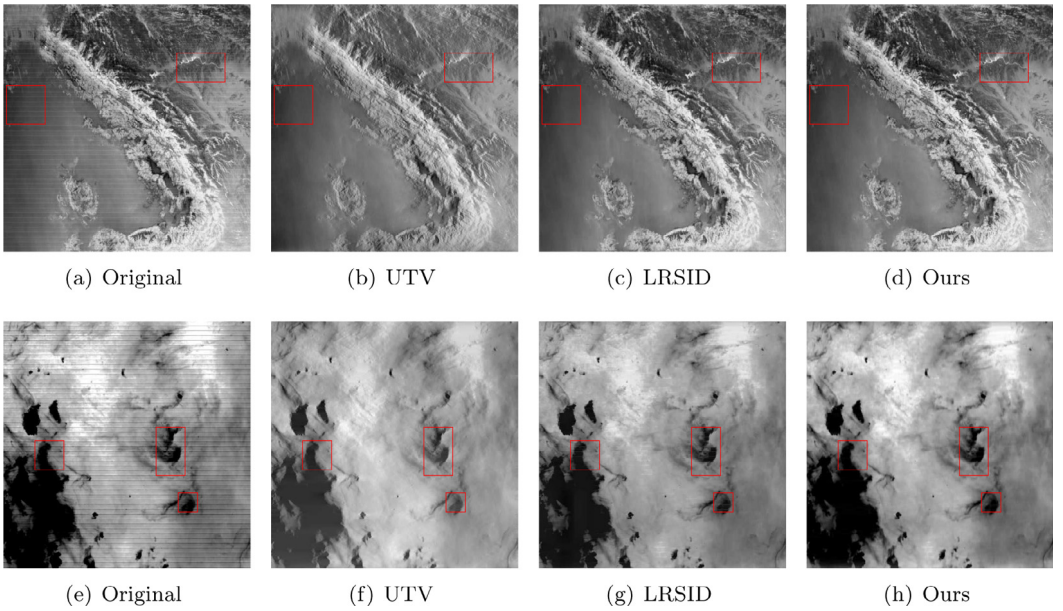

(a) Original (b) UTV (c) LRSID (d) Ours

(e) Original (f) UTV (g) LRSID (h) Ours

Fig. 14. Top row: destriping results of periodic stripes in Terra MODIS band 30. Bottom row: destriping results of periodic stripes in Terra MODIS band 27.

Table 2
PSNR (dB) results of the test methods for different stripe noise.

Image	Method	Stripe noise											
		Intensity = 10			Intensity = 50			Intensity = 0–50			Intensity = 100		
		r = 0.2	r = 0.6	r = 0.8	r = 0.2	r = 0.6	r = 0.8	r = 0.2	r = 0.6	r = 0.8	r = 0.2	r = 0.6	r = 0.8
Hyperspectral	Degraded	35.22	30.45	29.20	21.24	16.47	15.22	26.43	21.41	20.33	15.22	10.45	9.20
Periodical	UTV	43.84	43.34	44.15	38.03	37.74	38.95	38.28	36.08	34.48	36.87	36.22	37.53
Image	LRSID	42.98	44.00	45.56	37.59	**39.18**	40.38	37.06	34.71	32.5	35.49	37.13	38.54
	Proposed	**43.84**	**44.23**	**46.21**	**39.11**	38.46	**42.39**	**38.9**	**36.4**	**34.87**	**37.66**	**38.04**	**40.62**
Hyperspectral	Degraded	35.14	30.34	29.10	21.16	16.35	15.12	25.86	21.84	20.21	15.14	10.34	9.10
Non-Periodical	UTV	39.68	37.64	36.56	31.70	29.03	27.23	33.63	32.34	30.42	27.96	24.61	23.79
Image	LRSID	40.39	38.26	37.08	31.97	32.16	27.56	32.94	31.17	29.68	28.73	25.79	24.3
	Proposed	**42.1**	**39.65**	**38.24**	**34.65**	**32.63**	**31.44**	**36.22**	**35.68**	**34.22**	**32.44**	**29.6**	**29.62**
MODIS	Degraded	35.22	30.45	29.20	21.24	16.47	15.22	26.43	21.41	20.33	15.22	10.45	9.20
Periodical	UTV	37.86	37.51	37.64	36.07	35.52	35.80	36.23	33.75	34.33	34.97	34.40	34.84
Image	LRSID	43.31	43.29	43.44	38.40	40.43	41.60	39.35	34.89	34.90	38.60	39.64	41.77
	Proposed	**45.03**	**45.48**	**46.00**	**41.01**	**41.92**	**43.99**	**40.91**	**36.08**	**36.03**	**40.36**	**40.30**	**41.93**
MODIS	Degraded	35.14	30.34	29.10	21.16	16.36	15.12	25.86	21.84	20.21	15.14	10.34	9.10
Non-Periodical	UTV	**42.72**	40.62	35.11	32.03	28.70	**27.13**	33.34	31.10	30.49	29.12	24.63	23.54
Image	LRSID	41.74	39.25	36.91	31.91	**30.10**	25.07	33.04	31.37	**30.90**	28.55	**25.55**	22.83
	Proposed	41.29	**40.64**	**37.32**	**32.11**	29.36	27.06	**33.75**	**31.63**	30.86	**29.27**	24.73	**23.75**

5.2. Parameters

In our model, there are three regularization parameters λ_1, λ_2, and λ_3. It is worth reminding that parameter λ_3 depends on the width of stripes, and larger values should be chosen for wider stripes. To show their effects on the destriping performance, we give an analysis by using a simulated experiment (two lines together, intensity = 10) as an example. In Figs. 20–22, we show the PSNR and SSIM values with respect to the parameters λ_1, λ_2, and λ_3, respectively. From Fig. 20, we can find that the PSNR curve ($\lambda_2 = 0.0006$ and $\lambda_3 = 0.0003$) reaches the highest point at $\lambda_1 = 0.28$, and the SSIM value tends to be stable when $\lambda_1 \in [0.2, 0.4]$. For robustness, we choose the optimal parameter λ_1 in the range $[0, 1]$. Similarly, we empirically set $\lambda_2 \in [0.0001, 0.01]$ and $\lambda_3 \in [0.0001, 0.01]$. The hand-tuned strategy is used for three regularization parameters as follows: (1) empirically fix $\lambda_2 = 0.001$ and $\lambda_3 = 0.0001$, tune $\lambda_1 = i * 10^{-1}$ $(i = 0, 1, \ldots, 10)$ for the highest PSNR value. (2) Then fix λ_1, tune $\lambda_2, \lambda_3 = i * 10^{-3} + j * 10^{-4}$ $(i, j = 0, 1, \ldots, 10)$ for the highest PSNR value.

Table 3
SSIM results of the test methods for different stripe noise.

Image	Method	Stripe noise											
		Intensity = 10			Intensity = 50			Intensity = 0–50			Intensity = 100		
		r = 0.2	r = 0.6	r = 0.8	r = 0.2	r = 0.6	r = 0.8	r = 0.2	r = 0.6	r = 0.8	r = 0.2	r = 0.6	r = 0.8
Hyperspectral	Degraded	0.964	0.898	0.872	0.651	0.373	0.320	0.851	0.636	0.602	0.405	0.151	0.122
Periodical	UTV	0.997	0.997	0.997	0.993	0.992	0.994	**0.995**	0.993	0.992	0.992	0.991	0.993
Image	LRSID	0.996	0.997	0.997	0.991	0.992	0.992	0.989	0.987	0.984	0.984	0.987	0.989
	Proposed	**0.997**	**0.997**	**0.998**	**0.994**	**0.992**	**0.996**	0.994	**0.993**	**0.992**	**0.992**	**0.993**	**0.995**
Hyperspectral	Degraded	0.968	0.913	0.887	0.685	0.406	0.344	0.845	0.680	0.612	0.460	0.165	0.122
Non-Periodical	UTV	0.995	0.992	0.992	0.980	0.969	0.954	0.982	0.980	0.975	0.954	0.922	0.889
Image	LRSID	0.994	0.993	0.991	0.982	0.982	0.967	0.973	0.957	0.955	0.966	0.935	0.902
	Proposed	**0.997**	**0.996**	**0.995**	**0.992**	**0.989**	**0.988**	**0.994**	**0.993**	**0.992**	**0.989**	**0.982**	**0.979**
MODIS	Degraded	0.888	0.719	0.666	0.404	0.145	0.116	0.677	0.371	0.345	0.201	0.045	0.035
Periodical	UTV	0.991	0.991	0.994	**0.991**	**0.990**	0.984	0.993	**0.992**	**0.993**	0.982	0.981	0.977
Image	LRSID	0.987	0.984	0.982	0.978	0.977	0.986	0.988	0.986	0.989	0.981	0.979	**0.995**
	Proposed	**0.993**	**0.993**	**0.994**	0.976	0.985	**0.993**	**0.993**	0.988	0.991	**0.988**	**0.989**	0.991
MODIS	Degraded	0.902	0.757	0.705	0.455	0.174	0.134	0.682	0.410	0.348	0.272	0.056	0.040
Non-Periodical	UTV	0.994	0.992	**0.994**	0.988	0.980	0.978	0.992	0.976	0.986	0.981	0.973	0.971
Image	LRSID	0.991	0.983	0.986	0.946	0.971	0.894	0.969	0.970	0.973	0.956	0.951	0.944
	Proposed	**0.996**	**0.995**	0.993	**0.990**	**0.984**	**0.985**	**0.992**	**0.987**	**0.987**	**0.984**	**0.983**	**0.987**

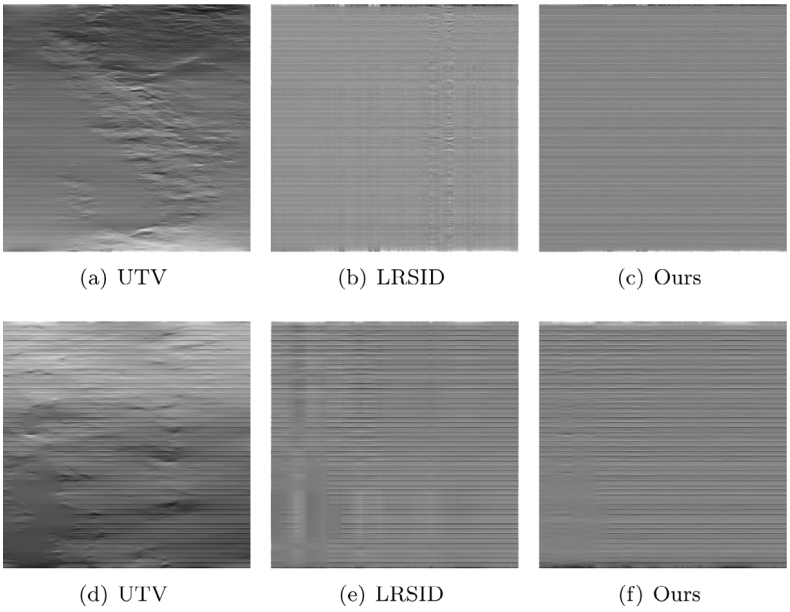

Fig. 15. Top row: stripe components of Terra MODIS band 30. Bottom row: stripe components of Terra MODIS band 27.

5.3. Numerical convergence of the proposed algorithm

To numerically illustrate the convergence of the proposed algorithm, we test two images, the hyperspectral image of Washington DC Mall and Terra MODIS image band 32 degraded by stripe noise that every three lines are grouped (intensity = 10). Fig. 23 shows the relative error curves of the successive restored image U^k and U^{k+1}, i.e., $\|U^{k+1} - U^k\|_F / \|U^k\|_F$. From Fig. 23, we can observe that the relative error keeps decreasing as the iteration number increases and our algorithm is convergent numerically.

5.4. Oblique stripe

The proposed model not only can handle the vertical stripes, but also can work on the oblique stripe with the aid of the shear operator [48]. We first use the shear operator to straighten the oblique stripe (see Fig. 24(c)), and then use the proposed method and compared methods to deal with the straightened image. Finally, the restored image is obtained by using the inverse shear operator. Fig. 24 shows the destriping results of three methods for the oblique stripe. Visually, we

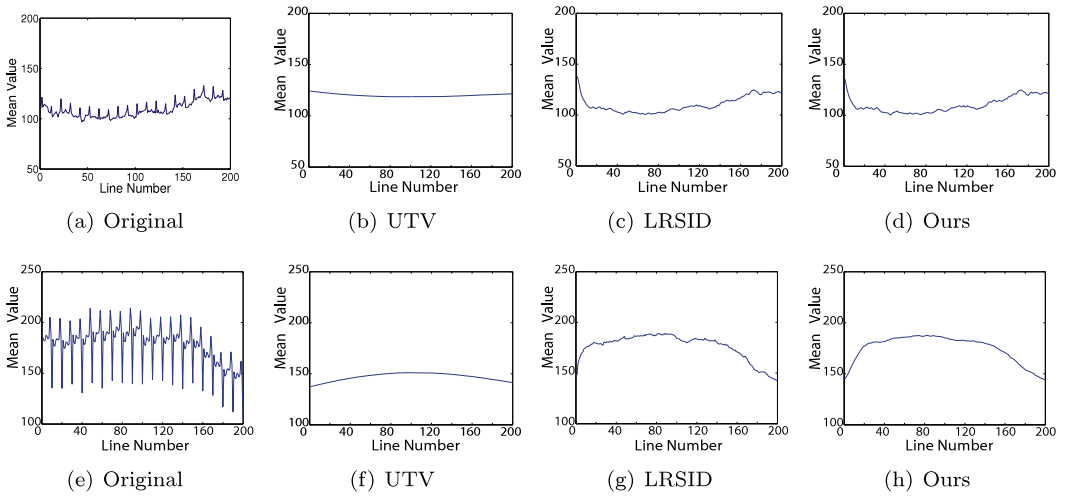

Fig. 16. Column mean cross-track profiles of Fig. 14.

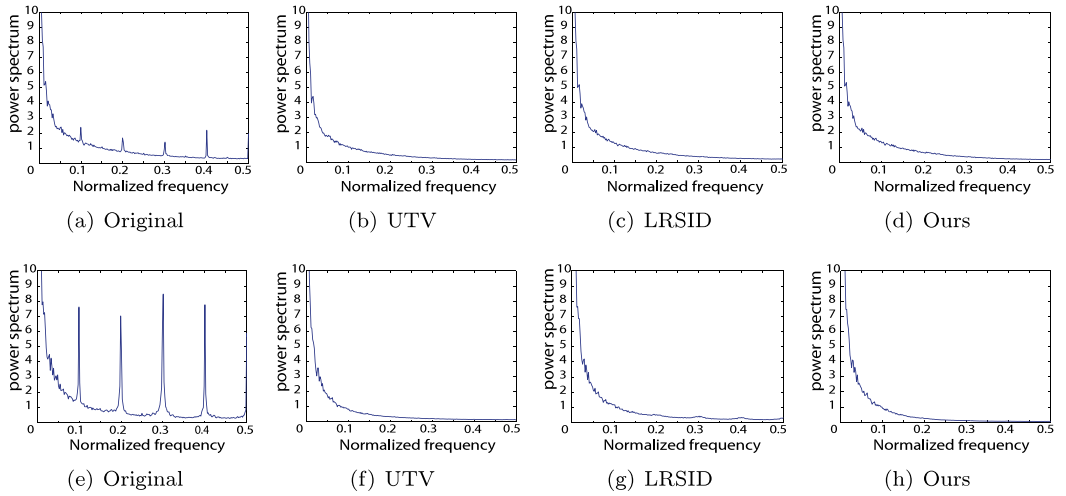

Fig. 17. Power spectrums of Fig. 14.

Table 4
Quantitative indices (NR, MRD, ICV, and Time (in seconds)) of the test methods for real experiments.

Image	Index	UTV	LRSID	Proposed
Terra MODIS band 30	NR	1.4349	1.1662	1.2490
	MRD	0.0836	0.0184	0.0192
	ICV	11.8818	9.3914	10.2635
	Time	1.46	35.00	52.30
Terra MODIS band 27	NR	1.8431	1.3575	1.9909
	MRD	0.1670	0.0673	0.0649
	ICV	48.0788	34.2230	33.6266
	Time	1.41	31.71	52.13
Terra MODIS band 33	NR	1.0192	1.5601	1.0984
	MRD	0.3420	0.0494	0.0415
	ICV	15.2490	4.4345	30.5643
	Time	0.89	20.07	29.36

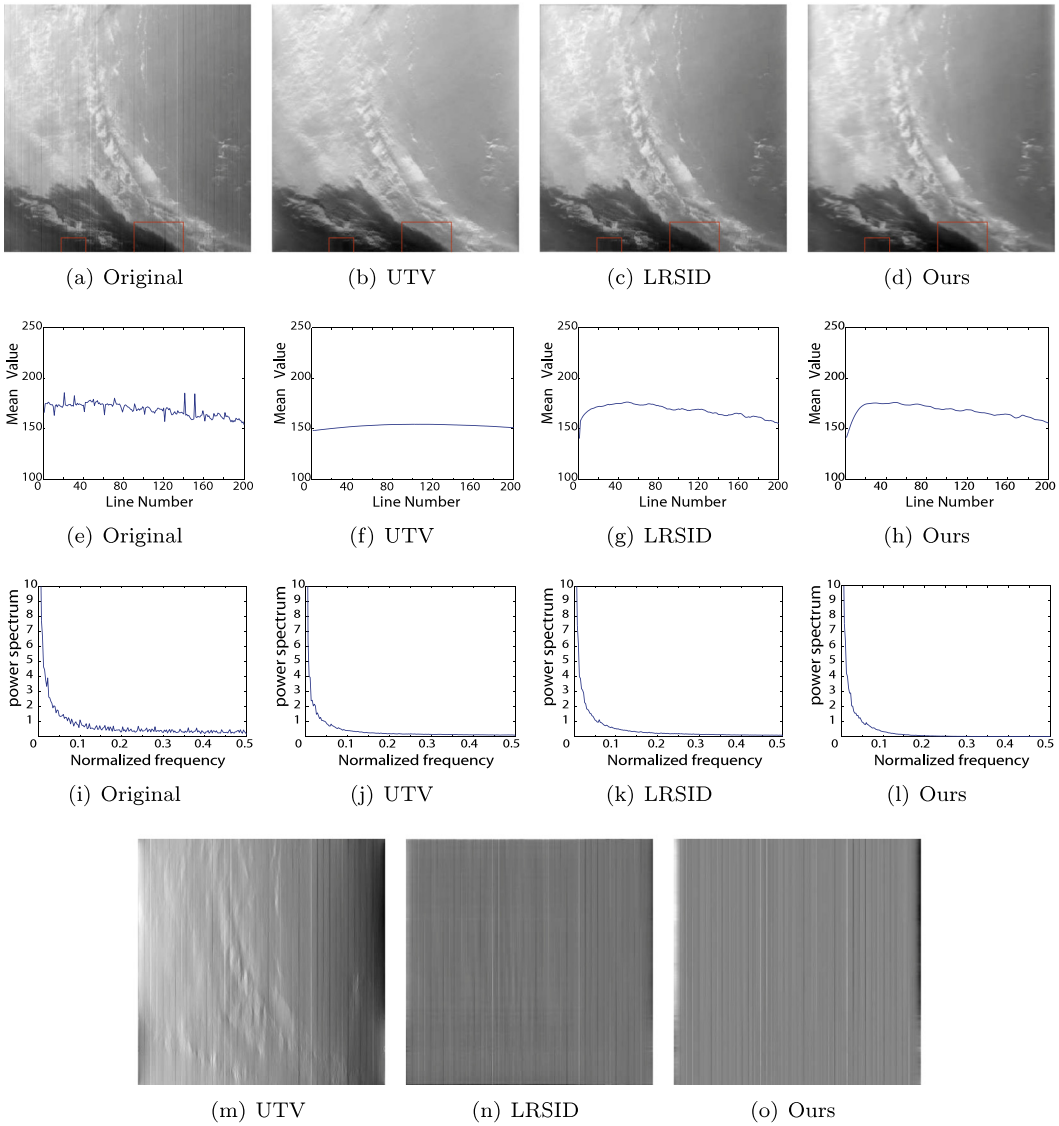

Fig. 18. Destriping results of nonperiodic stripes in Terra MODIS band 33. The first row: destriping results. The second row: column mean cross-track profiles. The third row: power spectrums. The fourth row: stripe components.

can observe that the proposed method is able to remove the oblique stripe in contrast with UTV and LRSID. Moreover, the performance of the proposed method is better than UTV and LRSID in terms of PSNR values.

6. Conclusions

In this work, we propose a novel model to remove stripe noise from remote sensing images. The proposed model uses UTV and UHTV to ensure the smoothness of the image, and uses the Schatten 1/2-norm to restrain the low-rankness of stripes. Besides, based on the framework of ADMM, we present an efficient algorithm to solve the proposed model. Experiments using both simulated and real data demonstrate the effectiveness of the proposed model to remove stripe noise in visual quality and quantitative indexes.

In addition, the proposed method not only works well on horizontal and vertical stripes, but works on oblique stripes. In future work, we will consider generalized mixed noise [49].

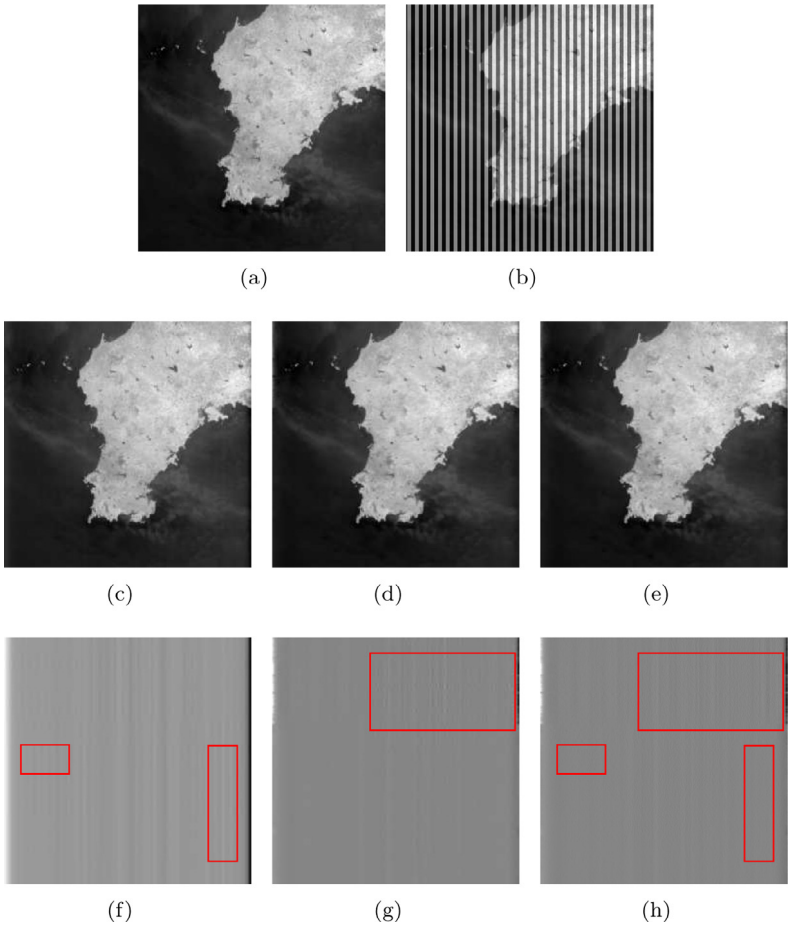

Fig. 19. Effectiveness of the proposed method (the stripe noise of four lines together, intensity = 100). Top row: (a) the original image, (b) the degraded image. Middle row: the recovered images. (c) The proposed method without the UHTV, (d) the nuclear norm instead of the Schatten 1/2-norm in the proposed method, (e) the proposed method. Bottom row: the residual error images. (f) The residual image of (c), (g) the residual image of (d), (h) the residual image of (e).

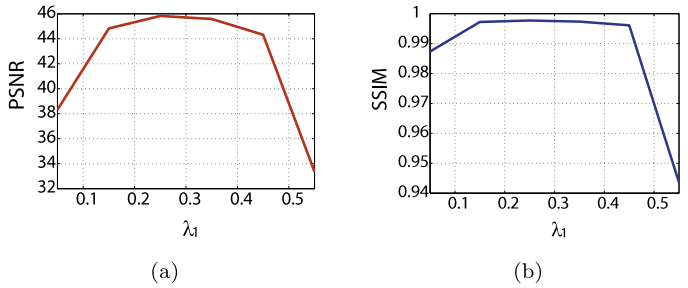

Fig. 20. The behavior of (a) PSNR values and (b) SSIM values with respect to the regularization parameter λ_1.

Acknowledgments

This research is supported by NSFC (61876203, 61772003), the Fundamental Research Funds for the Central Universities (ZYGX2016J132), National Postdoctoral Program for Innovative Talents (BX20180252), and Science Strength Promotion Programme of UESTC. We would like to thank Yi Chang for providing the codes of the method in [26].

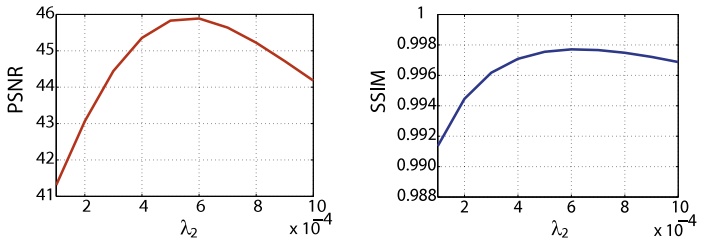

Fig. 21. The behavior of (a) PSNR values and (b) SSIM values with respect to the regularization parameter λ_2.

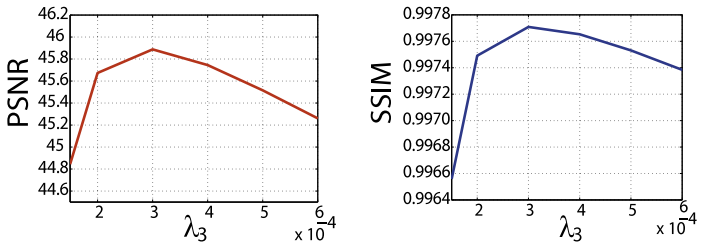

Fig. 22. The behavior of (a) PSNR values and (b) SSIM values with respect to the regularization parameter λ_3.

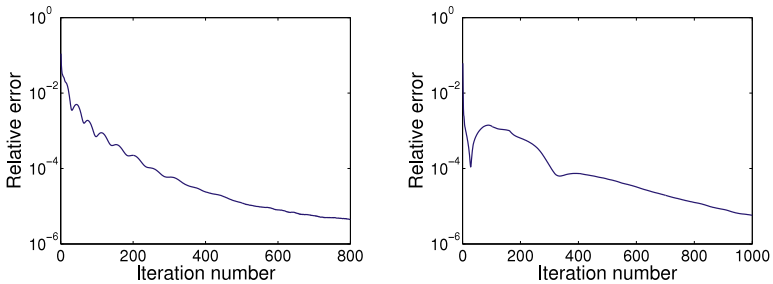

Fig. 23. Curves of relative error values versus iterations.

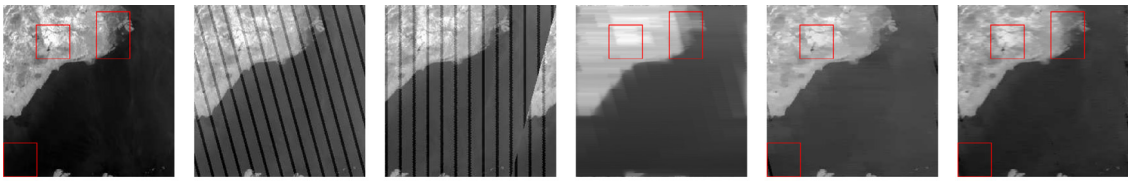

Fig. 24. Destriping results of different methods for the oblique stripe. The value in parentheses represents the corresponding PSNR (dB) value of the restored image.

References

[1] X.Q. Lu, Y.L. Wang, Y. Yuan, Graph-regularized low-rank representation for destriping of hyperspectral images, IEEE Trans. Geosci. Remote Sens. 51 (7) (2013) 4009–4018.

[2] Y.Z. Zhang, G. Zhou, L.X. Yan, T.X. Zhang, A destriping algorithm based on TV-stokes and unidirectional total variation model, Optik 127 (1) (2016) 428–439.

[3] H.Y. Zhang, J.Y. Li, Y.C. Huang, L.P. Zhang, A nonlocal weighted joint sparse representation classification method for hyperspectral imagery, IEEE J-Stars 7 (6) (2017) 2056–2065.

[4] Y. Tarabalka, J. Chanussot, J.A. Benediktsson, Segmentation and classification of hyperspectral images using watershed transformation, Pattern Recognit. 43 (7) (2010) 2367–2379.
[5] Z.G. Xiao, H. Chen, C.H. Tu, R. Klette, An effective graph and depth layer based RGB-D image foreground object extraction method, Comput. Vis. Med. 3 (4) (2017) 387–393.
[6] D.W.J. Stein, S.G. Beaven, L.E. Hoff, E.M. Winter, A.P. Schaum, A.D. Stocker, Anomaly detection from hyperspectral imagery, IEEE Signal Process. Mag. 19 (1) (2002) 58–69.
[7] A. Cuzzocrea, E. Mumolo, G.M. Grasso, Advanced pattern recognition from complex environments: a classification-based approach, Soft Comput. (6) (2017) 1–16.
[8] J.G. Liu, G.L.K. Morgan, FFT selective and adaptive filtering for removal of systematic noise in ETM+ imageodesy images, IEEE Trans. Geosci. Remote Sens. 44 (12) (2006) 3716–3724.
[9] R. Pande-Chhetri, A. Abd-Elrahman, De-striping hyperspectral imagery using wavelet transform and adaptive frequency domain filtering, ISPRS J. Photogramm. 66 (5) (2011) 620–636.
[10] J. Torres, S.O. Infante, Wavelet analysis for the elimination of striping noise in satellite images, Opt. Eng. 40 (7) (2001) 1309–1314.
[11] B.K.P. Horn, R.J. Woodham, Destriping Landsat MSS images by histogram modification, Comput. Graph. Image Process. 10 (1) (1979) 69–83.
[12] W. Michael, Destriping multiple sensor imagery by improved histogram matching, Int. J. Remote Sens. 11 (5) (1990) 859–875.
[13] F.L. Gadallah, F. Csillag, E.J.M. Smith, Destriping multisensor imagery with moment matching, Int. J. Remote Sens. 21 (12) (2000) 2505–2511.
[14] T. Mach, L. Reichel, M.V. Barel, R. Vandebril, Adaptive cross approximation for ill-posed problems, J. Comput. Appl. Math. 303 (C) (2016) 206–217.
[15] Y.T. Wang, X.L. Zhao, T.X. Jiang, L.J. Deng, Y.T. Zhang, A total variation and group sparsity based tensor optimization model for video rain streak removal, Signal Process. Image Commun. 73 (2019) 96–108.
[16] X. Zhou, F.G. Zhou, X.Z. Bai, B.D. Xue, A boundary condition based deconvolution framework for image deblurring, J. Comput. Appl. Math. 261 (4) (2014) 14–29.
[17] C. Matonoha, S. Papáček, On the connection and equivalence of two methods for solving an ill-posed inverse problem based on frap data, J. Comput. Appl. Math. 290 (2015) 598–608.
[18] L.J. Deng, T.Z. Huang, X.L. Zhao, T.X. Jiang, A directional global sparse model for single image rain removal, Appl. Math. Model. 59 (2018) 662–679.
[19] L.B. Cui, M.H. Li, Y.S. Song, Preconditioned tensor splitting iterations method for solving multi-linear systems, Appl. Math. Lett. 96 (2019) 89–94.
[20] H.F. Shen, L.P. Zhang, A MAP-based algorithm for destriping and inpainting of remotely sensed images, IEEE Trans. Geosci. Remote Sens. 47 (5) (2009) 1492–1502.
[21] M. Bouali, S. Ladjal, Toward optimal destriping of MODIS data using a unidirectional variational model, IEEE Trans. Geosci. Remote Sens. 49 (8) (2011) 2924–2935.
[22] G. Zhou, H.Z. Fang, C. Lu, S.Y. Wang, Z.Y. Zuo, J. Hu, Robust destriping of MODIS and hyperspectral data using a hybrid unidirectional total variation model, Optik 126 (7) (2015) 838–845.
[23] Y. Chang, H. Fang, L. Yan, H. Liu, Robust destriping method with unidirectional total variation and framelet regularization, Opt. Express 21 (20) (2013) 23307–23323.
[24] X.X. Liu, X.L. Lu, H.F. Shen, Q.Q. Yuan, Y.L. Jiao, L.P. Zhang, Stripe noise separation and removal in remote sensing images by consideration of the global sparsity and local variational properties, IEEE Trans. Geosci. Remote Sens. 54 (5) (2016) 3049–3060.
[25] Y. Chen, T.Z. Huang, X.L. Zhao, Destriping of multispectral remote sensing image using low-rank tensor decomposition, IEEE J-Stars 11 (12) (2018) 4950–4967.
[26] Y. Chang, L.X. Yan, T. Wu, S. Zhong, Remote sensing image stripe noise removal: From image decomposition perspective, IEEE Trans. Geosci. Remote Sens. 54 (12) (2016) 7018–7031.
[27] Z.B. Xu, H. Zhang, Y. Wang, X.Y. Chang, Y. Liang, $L_{1/2}$ Regularization, Sci. China Inf. Sci. 53 (6) (2010) 1159–1169.
[28] X.L. Zhao, F. Wang, M.K. Ng, A new convex optimization model for multiplicative noise and blur removal, SIAM J. Imaging Sci. 7 (1) (2014) 456–475.
[29] X.L. Zhao, W. Wang, T.Y. Zeng, T.Z. Huang, M.K. Ng, Total variation structured total least squares method for image restoration, SIAM J. Sci. Comput. 35 (6) (2013) 1304–1320.
[30] J.C.D.L. Reyes, C.B. Schönlieb, T. Valkonen, Bilevel parameter learning for higher-order total variation regularisation models, J. Math. Imaging Vision 57 (1) (2017) 1–25.
[31] S. Wang, T.Z. Huang, X.L. Zhao, J.J. Mei, J. Huang, Speckle noise removal in ultrasound images by first-order and second-order total variation, Numer. Algorithms (2017) 1–21.
[32] D. Lazzaro, L.B. Montefusco, Edge-preserving wavelet thresholding for image denoising, J. Comput. Appl. Math. 210 (1–2) (2007) 222–231.
[33] T. Chan, A. Marquina, P. Mulet, High-order total variation-based image restoration, SIAM J. Sci. Comput. 22 (2) (2000) 503–516.
[34] M. Benning, C. Brune, M. Burger, J. Müller, Higher-order TV methods - enhancement via Bregman iteration, J. Sci. Comput. 54 (2–3) (2013) 269–310.
[35] L.Z. Deng, Q. Fang, H. Zhu, G. Zhou, Image denoising based on spatially adaptive high order total variation model, in: CISP-BMEI, 2017, pp. 212–216.
[36] M. Ding, T.Z. Huang, S. Wang, J.J. Mei, X.L. Zhao, Total variation with overlapping group sparsity for deblurring images under Cauchy noise, Appl. Math. Comput. 341 (2019) 128–147.
[37] T.H. Ma, Y.F. Lou, T.Z. Huang, Truncated l_{1-2} models for sparse recovery and rank minimization, SIAM J. Imaging Sci. 10 (3) (2017) 1346–1380.
[38] S. Boyd, N. Parikh, E. Chu, B. Peleato, J. Eckstein, Distributed optimization and statistical learning via the alternating direction method of multipliers, Found. Trends Mach. Learn. 3 (1) (2011) 1–122.
[39] T. Goldstein, B. O'Donoghue, S. Setzer, R. Baraniuk, Fast alternating direction optimization methods, SIAM J. Imaging Sci. 7 (3) (2014) 1588–1623.
[40] T.X. Jiang, T.Z. Huang, X.L. Zhao, L.J. Deng, Y. Wang, A novel video rain streak removal method using directional gradient priors, IEEE Trans. Image Process. 28 (4) (2019) 2089–2102.
[41] Y.B. Zheng, T.Z. Huang, T.Y. Ji, X.L. Zhao, T.X. Jiang, T.H. Ma, Low-rank tensor completion via smooth matrix factorization, Appl. Math. Model. 70 (2019) 677–695.
[42] Z. Xu, X. Chang, F. Xu, H. Zhang, $L_{1/2}$ Regularization: a thresholding representation theory and a fast solver, IEEE Trans. Neural Netw. Learn. 23 (7) (2012) 1013–1027.
[43] J.S. Zeng, S.B. Lin, Y. Wang, Z.B. Xu, $L_{1/2}$ Regularization: Convergence of iterative Half thresholding algorithm, IEEE Trans. Signal Process. 62 (9) (2014) 2317–2329.
[44] D.L. Donoho, De-noising by soft-thresholding, IEEE Trans. Inform. Theory 41 (3) (2002) 613–627.
[45] J. Huang, T.Z. Huang, X.L. Zhao, Z.B. Xu, X.G. Lv, Two soft-thresholding based iterative algorithms for image deblurring, Inform. Sci. 271 (7) (2014) 179–195.
[46] W.M. Zuo, Z.C. Lin, A generalized accelerated proximal gradient approach for total-variation-based image restoration, IEEE Trans. Image Process. 20 (10) (2011) 2748–2759.

[47] R.W. Liu, L. Shi, W. Huang, J. Xu, S.C. Yu, D. Wang, Generalized total variation-based MRI Rician denoising model with spatially adaptive regularization parameters, Magn. Reson. Imaging 32 (6) (2014) 702–720.
[48] M.P. Weinreb, R. Xie, J.H. Lienesch, D.S. Crosby, Destriping GOES images by matching empirical distribution functions, Remote Sens. Environ. 29 (2) (1989) 185–195.
[49] Y. Chen, T.Z. Huang, X.L. Zhao, L.J. Deng, Hyperspectral image restoration using framelet-regularized low-rank nonnegative matrix factorization, Appl. Math. Model. 63 (2018) 128–147.